Letter

Open momentum space method for the Hofstadter butterfly and the quantized Lorentz susceptibility

Biao Lian, Fang Xie, and B. Andrei Bernevig
Department of Physics, Princeton University, Princeton, New Jersey 08544, USA

(Received 14 February 2021; accepted 9 April 2021; published 20 April 2021)

We develop a generic $\mathbf{k}\cdot\mathbf{p}$ open momentum space method for calculating the Hofstadter butterfly of both continuum (moiré) models and tight-binding models, where the quasimomentum is directly substituted by the Landau level (LL) operators. By taking a LL cutoff (and a reciprocal lattice cutoff for continuum models), one obtains the Hofstadter butterfly with in-gap spectral flows. For continuum models such as the moiré model for twisted bilayer graphene, our method gives a sparse Hamiltonian, making it much more efficient than existing methods. The spectral flows in the Hofstadter gaps can be understood as edge states on a momentum space boundary, from which one can determine the two integers (t_ν, s_ν) of a gap ν satisfying the Diophantine equation. The spectral flows can also be removed to obtain a clear Hofstadter butterfly. While t_ν is known as the Chern number, our theory identifies s_ν as a dual Chern number for the momentum space, which corresponds to a quantized Lorentz susceptibility $\gamma_{xy} = eBs_\nu$.

DOI: 10.1103/PhysRevB.103.L161405

Two-dimensional (2D) lattice electrons in large magnetic fields are known to exhibit Hofstadter butterfly spectra [1]. Conventionally, the Hofstadter butterfly is calculated at rational fluxes per unit cell $\varphi = 2\pi p/q$ in a basis with translation symmetry of q unit cells, where p and q are coprime integers. The calculation often involves a complicated construction of the matrix elements. In particular, for continuum $\mathbf{k}\cdot\mathbf{p}$ models obtained from plane-wave expansions such as the moiré model for twisted bilayer graphene (TBG) [2–4], the Hofstadter Hamiltonian matrix is infinite dimensional and dense [5–10], which requires a large cutoff for the spectrum to converge.

In contrast, the Landau levels (LLs) of a $\mathbf{k}\cdot\mathbf{p}$ Hamiltonian at small magnetic fields can be calculated by simply substituting the quasimomentum $\mathbf{k} = (k_x, k_y)$ with $(\frac{a+a^\dagger}{\sqrt{2}\ell}, \frac{a-a^\dagger}{i\sqrt{2}\ell})$, where a and $a^\dagger$ are the LL lowering and raising operators, and ℓ is the magnetic length [11]. In this Letter, we demonstrate that such a substitution with a LL cutoff (and a reciprocal lattice cutoff for continuum models) provides an efficient method for calculating the Hofstadter butterfly in large magnetic fields, which greatly simplifies the Hamiltonian matrix elements [12]. In particular, for continuum models, this method yields a sparse Hamiltonian, whose spectrum can be efficiently calculated by the shift-and-invert Lanczos method.

The method can be understood as an open momentum space calculation, where the smaller of the momentum space LL wave-function radius cutoff and reciprocal lattice radius cutoff plays the role of a momentum space boundary. As a result, the spectrum contains not only the Hofstadter butterfly, but also in-gap spectral flow levels [12,13] which can be understood as "momentum space edge states." We show that the spectral flows of these edges allow us to determine the two integers (t_ν, s_ν) in a Hofstadter gap ν satisfying the Diophantine equation [14–16], where t_ν is the Chern number of the gap. Moreover, we show that s_ν can be interpreted as a dual Chern number for the momentum space, which yields a quantized Lorentz susceptibility [Eq. (15)]. Furthermore, by identifying and removing the momentum space edge states, one can obtain the Hofstadter butterfly without spectral flows. We demonstrate our method for both continuum models and tight-binding models in a 2D periodic lattice. We shall denote the lattice Bravais vectors as $\boldsymbol{d}_1$ and $\boldsymbol{d}_2$, and the reciprocal vectors as $\boldsymbol{g}_1$ and $\boldsymbol{g}_2$, which satisfy $\boldsymbol{g}_i \cdot \boldsymbol{d}_j = 2\pi\delta_{ij}$ $(i, j = 1, 2)$.

Continuum models. At zero magnetic field, a continuum model can be written in the real space basis $|\mathbf{r}, \alpha\rangle$ as [3–7,17]

$$H^{\alpha\beta}(\mathbf{r}) = \epsilon^{\alpha\beta}(-i\nabla) + \sum_j V_j^{\alpha\beta} e^{i\mathbf{q}_j^{\alpha\beta}\cdot\mathbf{r}}, \tag{1}$$

where $\mathbf{r} = (x, y)$ is the real space position, $-i\nabla = -i(\partial_x, \partial_y)$ is the canonical momentum, and we assume there are M intrinsic orbitals labeled by α, β. $\epsilon^{\alpha\beta}(-i\nabla)$ and $V_j^{\alpha\beta} e^{i\mathbf{q}_j^{\alpha\beta}\cdot\mathbf{r}}$ are the electron kinetic term in free space and the periodic lattice potential between orbitals β and α, respectively. If one denotes $\mathbf{Q} \in \boldsymbol{g}_1\mathbb{Z} + \boldsymbol{g}_2\mathbb{Z}$ as the reciprocal lattice, and chooses the momentum origin of orbital α at $\mathbf{p}_\alpha$, one can define a momentum lattice $\mathbf{Q}_\alpha = \mathbf{p}_\alpha + \mathbf{Q}$ for orbital α, and $\mathbf{q}_j^{\alpha\beta}$ in Eq. (1) must be the difference $\mathbf{Q}'_\alpha - \mathbf{Q}_\beta$ between some sites $\mathbf{Q}'_\alpha$ and $\mathbf{Q}_\beta$ [see Supplemental Material (SM) [18] Sec. S2A]. Generically, one can always fix all $\mathbf{p}_\alpha = \mathbf{0}$; however, in certain models (e.g., the TBG model [2]) nonzero $\mathbf{p}_\alpha$ choices are preferred.

One can transform the zero-magnetic-field Hamiltonian (1) into the momentum eigenbasis $|\mathbf{k}, \mathbf{Q}_\alpha, \alpha\rangle = \int d^2\mathbf{r} e^{i(\mathbf{k}+\mathbf{Q}_\alpha)\cdot\mathbf{r}} |\mathbf{r}, \alpha\rangle$, where $\mathbf{k}$ is in the first Brillouin zone (BZ). The momentum space Hamiltonian under basis

$|\mathbf{k}, \mathbf{Q}_\alpha, \alpha\rangle$ then takes the form [2,18]

$$H^{\alpha\beta}_{\mathbf{Q}'_\alpha\mathbf{Q}_\beta}(\mathbf{k}) = \epsilon^{\alpha\beta}(\mathbf{k}+\mathbf{Q}_\beta)\delta_{\mathbf{Q}'_\alpha\mathbf{Q}_\beta} + \sum_j V_j^{\alpha\beta}\delta_{\mathbf{Q}'_\alpha,\mathbf{Q}_\beta+\mathbf{q}_j^{\alpha\beta}}. \quad (2)$$

When a uniform out-of-plane magnetic field $\mathbf{B} = B\hat{\mathbf{z}}$ is added, $-i\nabla$ in Eq. (1) is replaced by the kinematic momentum $\mathbf{\Pi} = -i\nabla - \mathbf{A}(\mathbf{r})$, where $\mathbf{A}(\mathbf{r})$ is the vector potential satisfying $\partial_x A_y - \partial_y A_x = B$. The kinetic momentum satisfies $[\Pi_x, \Pi_y] = i/\ell^2$, where $\ell = 1/\sqrt{B}$ is the magnetic length. We also define the guiding center $\mathbf{R} = \mathbf{r} - \ell^2\hat{\mathbf{z}} \times \mathbf{\Pi}$, which satisfies $[R_x, R_y] = -i\ell^2$, and $[\mathbf{R}, \mathbf{\Pi}] = \mathbf{0}$.

The usual Hofstadter method for continuum models employs the Landau basis defined by eigenstates of R_x and $\mathbf{\Pi}^2$, which has complicated matrix elements [5–10]. Here, we shall take a different basis, under which we prove the nonzero-magnetic-field Hamiltonian can be simply obtained by the zero-field momentum space Hamiltonian (2) with the substitution of Eq. (5).

We define $R_{\hat{\boldsymbol{\tau}}} = \mathbf{R}\cdot\hat{\boldsymbol{\tau}}$ as the guiding center along unit vector $\hat{\boldsymbol{\tau}}$, where we choose $\frac{\hat{\boldsymbol{\tau}}\cdot(\hat{\mathbf{z}}\times\boldsymbol{g}_1)}{\hat{\boldsymbol{\tau}}\cdot(\hat{\mathbf{z}}\times\boldsymbol{g}_2)}$ irrational. We also define a set of (linearly dependent) LL operators $a_{\mathbf{Q}_\alpha} = \frac{\ell}{\sqrt{2}}[\Pi_x - Q_{\alpha,x} - k_{0,x} + i(\Pi_y - Q_{\alpha,y} - k_{0,y})]$ and their conjugates $a^\dagger_{\mathbf{Q}_\alpha}$ associated with momentum sites $\mathbf{Q}_\alpha$, where $\mathbf{k}_0 = (k_{0,x}, k_{0,y})$ is a freely chosen real vector which we call the *center momentum*. We then construct an orthonormal basis $|\lambda, \mathbf{Q}_\alpha, n, \alpha\rangle$ for orbital α and reciprocal site $\mathbf{Q}_\alpha$ by requiring

$$R_{\hat{\boldsymbol{\tau}}}|\lambda, \mathbf{Q}_\alpha, n, \alpha\rangle = [\lambda - \ell^2\hat{\boldsymbol{\tau}}\cdot(\hat{\mathbf{z}}\times\mathbf{Q}_\alpha)]|\lambda, \mathbf{Q}_\alpha, n, \alpha\rangle,$$
$$a^\dagger_{\mathbf{Q}_\alpha}a_{\mathbf{Q}_\alpha}|\lambda, \mathbf{Q}_\alpha, n, \alpha\rangle = n|\lambda, \mathbf{Q}_\alpha, n, \alpha\rangle. \quad (3)$$

Here, $n \geqslant 0$ is an integer LL number, while λ is a real number chosen in the set $\lambda + \ell^2\hat{\boldsymbol{\tau}}\cdot(\hat{\mathbf{z}}\times\boldsymbol{g}_1)\mathbb{Z} + \ell^2\hat{\boldsymbol{\tau}}\cdot(\hat{\mathbf{z}}\times\boldsymbol{g}_2)\mathbb{Z}$ representing the set, or abstractly, $\lambda \in \mathbb{R}/[\ell^2\hat{\boldsymbol{\tau}}\cdot(\hat{\mathbf{z}}\times\boldsymbol{g}_1)\mathbb{Z} + \ell^2\hat{\boldsymbol{\tau}}\cdot(\hat{\mathbf{z}}\times\boldsymbol{g}_2)\mathbb{Z}]$ (see SM [18] Sec. S2B). It can then be proved that all the states $|\lambda, \mathbf{Q}_\alpha, n, \alpha\rangle$ form a complete basis for the continuum model satisfying $\langle\lambda, \mathbf{Q}_\alpha, n, \alpha|\lambda', \mathbf{Q}'_\beta, n', \beta\rangle = \delta_{\lambda\lambda'}\delta_{\mathbf{Q}_\alpha,\mathbf{Q}'_\beta}\delta_{nn'}\delta_{\alpha\beta}$.

The above basis $|\lambda, \mathbf{Q}_\alpha, n, \alpha\rangle$ is advantageous because the nonzero-magnetic-field Hamiltonian is diagonal in λ and independent of λ. In SM [18] Sec. S2B, we show the Hamiltonian in a fixed λ subspace is

$$H^{\lambda,\alpha\beta}_{\mathbf{Q}'_\alpha\mathbf{Q}_\beta} = \epsilon^{\alpha\beta}(\hat{\boldsymbol{\kappa}}_{\mathbf{Q}_\beta} + \mathbf{k}_0 + \mathbf{Q}_\beta)\delta_{\mathbf{Q}'_\alpha\mathbf{Q}_\beta} + \sum_j V_j\delta_{\mathbf{Q}'_\alpha,\mathbf{Q}_\beta+\mathbf{q}_j^{\alpha\beta}}, \quad (4)$$

where we have defined $\hat{\boldsymbol{\kappa}}_{\mathbf{Q}_\alpha} = \frac{1}{\sqrt{2}\ell}(a_{\mathbf{Q}_\alpha} + a^\dagger_{\mathbf{Q}_\alpha}, -ia_{\mathbf{Q}_\alpha} + ia^\dagger_{\mathbf{Q}_\alpha})$. Without ambiguity, we can drop the subindex $\mathbf{Q}_\alpha$ and simplify $(a_{\mathbf{Q}_\alpha}, a^\dagger_{\mathbf{Q}_\alpha})$ as $(a, a^\dagger)$, which acts as $a|\lambda, \mathbf{Q}_\alpha, n, \alpha\rangle = \sqrt{n}|\lambda, \mathbf{Q}_\alpha, n-1, \alpha\rangle$ and $a^\dagger|\lambda, \mathbf{Q}_\alpha, n, \alpha\rangle = \sqrt{n+1}|\lambda, \mathbf{Q}_\alpha, n+1, \alpha\rangle$. The Hamiltonian (4) is then exactly the zero-field Hamiltonian $H^{\alpha\beta}_{\mathbf{Q}'_\alpha\mathbf{Q}_\beta}(\mathbf{k})$ in Eq. (2) with the substitution

$$k_x \to \frac{a+a^\dagger}{\sqrt{2}\ell} + k_{0,x}, \quad k_y \to \frac{a-a^\dagger}{i\sqrt{2}\ell} + k_{0,y}, \quad (5)$$

as we claimed earlier. One then only need calculate the spectrum for a fixed λ. Different λ and λ' subspaces have identical spectra, but have eigenstates differing by displacement $\lambda - \lambda'$ in the $\hat{\boldsymbol{\tau}}$ direction ($R_{\hat{\boldsymbol{\tau}}}$ eigenvalue).

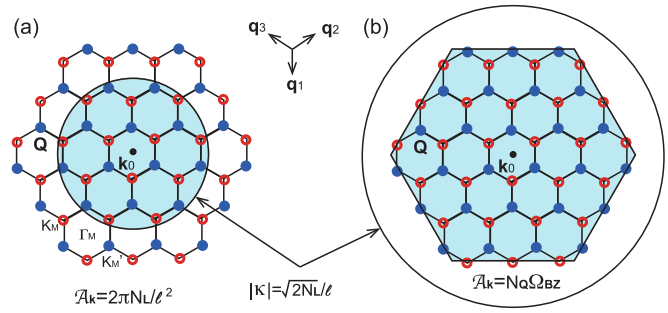

FIG. 1. (a) When $\varphi/2\pi < N_Q/N_L$, the momentum space (the shaded area) has a circular boundary of radius $\sqrt{2N_L}/\ell$. (b) When $\varphi/2\pi > N_Q/N_L$, the momentum space boundary is the reciprocal lattice boundary enclosing N_Q BZs (the shaded area).

To numerically calculate the spectrum of Hamiltonian (4), one can fix a center momentum $\mathbf{k}_0$, take a LL cutoff $n \leqslant N_L$, and take a cutoff of reciprocal lattice $\mathbf{Q}_\alpha$ at a boundary enclosing N_Q BZs. This yields a Hamiltonian of size MN_LN_Q for M intrinsic orbitals. If $\epsilon(\mathbf{k})$ only contains polynomials up to Δth power of $\mathbf{k}$, and the number of $\mathbf{q}_j^{\alpha\beta}$ is finite, $\langle\lambda, \mathbf{Q}'_\alpha, m, \alpha|H|\lambda, \mathbf{Q}_\beta, n, \beta\rangle$ will be zero for $|m-n| > \Delta$ or $|\mathbf{Q}'_\alpha - \mathbf{Q}_\beta| > \max(|\mathbf{q}_j^{\alpha\beta}|)$, so the Hamiltonian H is a sparse matrix. The low-energy eigenstates and spectrum can then be efficiently calculated by the Lanczos algorithm.

The cutoffs N_Q and N_L, however, lead to spectral flows in the Hofstadter gaps due to the absence of periodic boundary conditions [12,13]. As an example, we calculate the Hofstadter butterfly of the TBG continuum model defined on a honeycomb momentum lattice $\mathbf{Q}_\alpha$ [2], which has a Dirac kinetic term $\epsilon(\mathbf{k}) = v_F\boldsymbol{\sigma}^*\cdot\mathbf{k}$, and 2×2 hopping matrices V_j between the nearest momentum sites, where $\boldsymbol{\sigma}^* = (\sigma_x, -\sigma_y)$ are the Pauli matrices (SM [18] Sec. S3). Figure 2(a) shows the TBG spectrum at twist angle $\theta = 2.2^\circ$ versus the flux per unit cell $\varphi = B|\boldsymbol{d}_1 \times \boldsymbol{d}_2|$, where we take $N_Q = 37$ and $N_L = 60$. Besides the Hofstadter butterfly, one can see numerous in-gap spectral flow levels.

The in-gap spectral flows are generically due to the presence of boundaries which host edge states [12,13]. Here, as illustrated in Figs. 1(a) and 1(b), the cutoff N_Q sets a boundary of momentum radius $\sqrt{\frac{N_Q\Omega_{\mathrm{BZ}}}{\pi}}$ enclosing N_Q BZs, where $\Omega_{\mathrm{BZ}} = 4\pi^2/|\boldsymbol{d}_1 \times \boldsymbol{d}_2|$ is the BZ area, while the LL cutoff N_L yields a boundary $\sqrt{\langle\hat{\boldsymbol{\kappa}}^2_{\mathbf{Q}_\alpha}\rangle} \leqslant \frac{\sqrt{2N_L}}{\ell}$ for $\hat{\boldsymbol{\kappa}}_{\mathbf{Q}_\alpha}$ in the Hamiltonian (4). The smaller value of $\sqrt{\frac{N_Q\Omega_{\mathrm{BZ}}}{\pi}}$ and $\frac{\sqrt{2N_L}}{\ell}$ then serves as a momentum space boundary radius for Hamiltonian (4) (SM [18] Sec. S2C), which gives rise to edge states.

The momentum space edge state levels then generate the spectral flows versus the magnetic field B. This can be understood from the Diophantine equation [14–16,18] satisfied by the νth Hofstadter gap ($\nu \in \mathbb{Z}$) at $\varphi = 2\pi p/q$ flux per unit cell,

$$t_\nu p + s_\nu q = \nu, \quad (6)$$

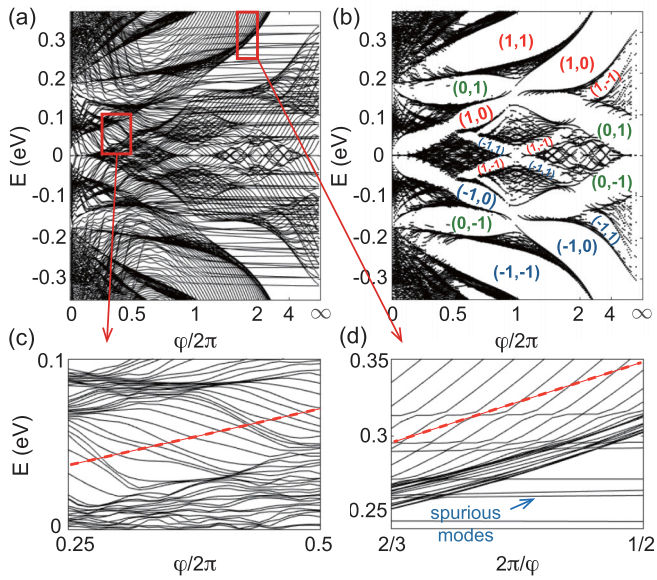

FIG. 2. (a) Hofstadter butterfly and spectral flow of $\theta = 2.2^\circ$ TBG with $N_Q = 37$ and $N_L = 60$, and $\mathbf{k}_0$ at the Γ point. The horizontal axis $\varphi/2\pi$ is linearly plotted in [0,1], and deformed into $2 - 2\pi/\varphi$ in $[1, \infty]$. (b) The Hofstadter butterfly after deleting the edge states (with $w = \min\{\ell^{-1}, 1.6\sqrt{\Omega_{\rm BZ}}\}$, $P_c = 0.5$), and (t_ν, s_ν) in the gaps. (c) Zoom-in plot in the regime $\varphi/2\pi < N_Q/N_L$. (d) Zoom-in plot in the regime $\varphi/2\pi > N_Q/N_L$.

where (t_ν, s_ν) are two integer quantum numbers characterizing the gap. t_ν is the Chern number of the gap, while s_ν is referred to as the electromechanical quantum number in Ref. [5]. It is often rewritten as

$$t_\nu \frac{\varphi}{2\pi} + s_\nu = \rho, \tag{7}$$

where $\rho = \nu/q$ is the number of occupied bulk states per unit cell in the gap [18–20]. Here, it is more useful to rewrite it in a dual form

$$t_\nu + s_\nu \frac{2\pi}{\varphi} = \rho_K, \tag{8}$$

where $\rho_K = 2\pi\rho/\varphi = \nu/p$. In SM [18] Sec. S2F, we show that ρ_K gives the number of occupied bulk states *per BZ* in the gap for the Hamiltonian (4) at a fixed λ. Furthermore, in Eq. (16), we show that s_ν plays the role of a dual Chern number for the momentum space. Equation (8) then determines the in-gap spectral flows [Fig. 2(a)] in two different regimes as follows.

In the first regime $\varphi/2\pi < N_Q/N_L$, the momentum space boundary is a circle enclosing a φ-dependent area $\mathcal{A}_K = 2\pi N_L/\ell^2$ centered at $\mathbf{k}_0$ [Fig. 1(a)]. In a gap, the total number of occupied states in the momentum area $\mathcal{A}_K$ is $\mathcal{N}_K = \rho_K \mathcal{A}_K/\Omega_{\rm BZ} = N_L\rho_K\varphi/2\pi = N_L\rho$. Therefore, by Eq. (8) we have

$$\mathcal{N}_K = N_L(t_\nu\varphi/2\pi + s_\nu). \tag{9}$$

In a bulk gap, the number of occupied states $\mathcal{N}_K$ can only change by pumping edge states into (out of) the bulk. Therefore, the edge states necessarily produce in-gap spectral flows, where the rate of flowing levels is $d\mathcal{N}_K/d(\varphi/2\pi) = N_L t_\nu$ by Eq. (9). Figure 2(c) shows a gap in this regime, where the midgap line (dashed line) crosses 16 levels as $\varphi/2\pi$ increases from 0.25 to 0.5, and $N_L = 60$. The flow rate is then $d\mathcal{N}_K/d(\varphi/2\pi) = 16/(0.5 - 0.25) = 64$, so we can identify the Chern number of the gap as the integer closest to $N_L^{-1} d\mathcal{N}_K/d(\varphi/2\pi) = 1.07$, namely, $t_\nu = 1$. Further, at $\varphi/2\pi = 0.5$, we counted there are $\mathcal{N}_K = 32$ levels from zero energy to the midgap energy [for TBG, $\mathcal{N}_K = 0$ is at zero energy (SM [18] Sec. S2G)], so we find the gap has $s_\nu = \mathcal{N}_K/N_L - t_\nu\varphi/2\pi = 0$ from Eq. (9).

In the second regime $\varphi/2\pi > N_Q/N_L$, the momentum space boundary is given by cutoff N_Q, which encloses a φ independent area $\mathcal{A}_K = N_Q\Omega_{\rm BZ}$ [Fig. 1(b)]. The number of occupied states $\mathcal{N}_K = \rho_K\mathcal{A}_K/\Omega_{\rm BZ}$ in momentum area $\mathcal{A}_K$ in a gap is then

$$\mathcal{N}_K = N_Q(t_\nu + 2\pi s_\nu/\varphi). \tag{10}$$

This yields a spectral flow rate $d\mathcal{N}_K/d(2\pi/\varphi) = N_Q s_\nu$. Besides, for TBG which has a Dirac kinetic term, there are $2N_Q$ horizontal levels at $\varphi/2\pi > N_Q/N_L$ in Fig. 2(a), which are spurious zero modes due to LL cutoff N_L (see SM [18] Sec. S3). These spurious levels should be excluded when counting $\mathcal{N}_K$. Figure 2(d) shows a gap in this regime, where the midgap line crosses six levels (excluding the spurious modes) as $2\pi/\varphi$ decreases from 2/3 to 1/2, and $N_Q = 37$. The flow rate is then $d\mathcal{N}_K/d(2\pi/\varphi) = 6/(2/3 - 1/2) = 36$, thus s_ν can be identified as the integer closest to $N_Q^{-1} d\mathcal{N}_K/d(2\pi/\varphi) = 0.97$, namely, $s_\nu = 1$. Further, we counted there are $\mathcal{N}_K = 55$ levels (excluding the spurious modes) between the midgap and zero energy at $2\pi/\varphi = 1/2$, thus the gap has a Chern number $t_\nu = \mathcal{N}_K/N_Q - 2\pi s_\nu/\varphi = 1$ from Eq. (10).

We note that models with a Dirac kinetic term $\epsilon(\mathbf{k}) = v_F\boldsymbol{\sigma}^* \cdot \mathbf{k}$ would have $\mathcal{N}_K = 0$ defined at half filling (zero energy for TBG), while models with a lower-bounded kinetic term [e.g., $\epsilon(\mathbf{k}) = k^2/2m_0$] would have $\mathcal{N}_K = 0$ below the lowest band (SM [18] Sec. S2G). More generically, if a gap persists below and above $\varphi/2\pi = N_Q/N_L$, one can identify t_ν and s_ν separately from the spectral flow rates at small and large φ, after which one can obtain $\mathcal{N}_K$ of the gap from Eq. (9) or (10).

The edge states and spurious modes can be easily removed from the spectrum. We define a boundary projector $P_{\kappa_b, w}$ onto basis $|\lambda, \mathbf{Q}_\alpha, n, \alpha\rangle$ with $n > (\kappa_b - w)^2\ell^2/2$ for some $w > 0$, where $\kappa_b \approx \min\{\frac{\sqrt{2N_L}}{\ell}, \sqrt{\frac{N_Q\Omega_{\rm BZ}}{\pi}}\}$ is the radius of momentum space boundary. We can then identify the eigenstates with $\langle P_{\kappa_b,w}\rangle > P_c$ above a certain value $P_c \in [0, 1]$ as momentum space edge states within distance w to the boundary, and delete them to obtain a bulk Hofstadter spectrum. For example, Fig. 2(b) is obtained by setting $w = \min\{\ell^{-1}, 1.6\sqrt{\Omega_{\rm BZ}}\}$ and $P_c = 0.5$.

Tight-binding models. The substitution (5) can also be employed to calculate the Hofstadter butterfly of tight-binding models. Given the position $\boldsymbol{u}_\alpha$ of each Wannier orbital α in a unit cell in the continuum space, we denote orbital α at position $\boldsymbol{D} + \boldsymbol{u}_\alpha$ as $|\boldsymbol{D}, \alpha\rangle$, where $\boldsymbol{D} \in \boldsymbol{d}_1\mathbb{Z} + \boldsymbol{d}_2\mathbb{Z}$ is the lattice vector. The Hamiltonian under Peierls substitution [21–23] then takes the form

$$H = \sum_{j,\alpha,\beta} t_j^{\alpha\beta} T_{\boldsymbol{D}_j + \boldsymbol{u}_\alpha - \boldsymbol{u}_\beta}, \tag{11}$$

where $\boldsymbol{D}_j \in \boldsymbol{d}_1\mathbb{Z} + \boldsymbol{d}_2\mathbb{Z}$, $t_j^{\alpha\beta}$ is the hopping from $|\boldsymbol{D}, \beta\rangle$ to $|\boldsymbol{D} + \boldsymbol{D}_j, \alpha\rangle$, and

$$T_{\boldsymbol{D}_j+\boldsymbol{u}_\alpha-\boldsymbol{u}_\beta} = \sum_{\boldsymbol{D}} e^{i\int_{c_{\alpha\beta}} \mathbf{A}(\mathbf{r})\cdot d\mathbf{r}} |\boldsymbol{D} + \boldsymbol{D}_j, \alpha\rangle\langle \boldsymbol{D}, \beta| \tag{12}$$

is the translation operator, with $c_{\alpha\beta}$ being the straight line segment from $\boldsymbol{D} + \boldsymbol{u}_\beta$ to $\boldsymbol{D} + \boldsymbol{D}_j + \boldsymbol{u}_\alpha$. At zero magnetic field, the Hamiltonian can be transformed into the momentum space basis $|\mathbf{k}, \alpha\rangle = \sum_{\boldsymbol{D}} e^{i\mathbf{k}\cdot(\mathbf{D}+\boldsymbol{u}_\alpha)}|\boldsymbol{D}, \alpha\rangle$ as

$$H^{\alpha\beta}(\mathbf{k}) = \sum_j t_j^{\alpha\beta} e^{-i\mathbf{k}\cdot(\boldsymbol{D}_j+\boldsymbol{u}_\alpha-\boldsymbol{u}_\beta)}. \tag{13}$$

At nonzero magnetic field, we define a basis as $\overline{|\lambda, n, \alpha\rangle} = \sum_{\boldsymbol{D}} |\boldsymbol{D}, \alpha\rangle\langle \boldsymbol{D} + \boldsymbol{u}_\alpha, \alpha|\lambda, \mathbf{0}, n, \alpha\rangle$, where $|\boldsymbol{D} + \boldsymbol{u}_\alpha, \alpha\rangle$ is the continuum space position eigenstate at position $\mathbf{r} = \boldsymbol{D} + \boldsymbol{u}_\alpha$, $|\lambda, \mathbf{0}, n, \alpha\rangle$ is the state defined in Eq. (3) in the continuum space at reciprocal site $\mathbf{0}$, and $\lambda \in \mathbb{R}/[\ell^2\hat{\boldsymbol{\tau}}\cdot(\hat{\mathbf{z}}\times\boldsymbol{g}_1)\mathbb{Z} + \ell^2\hat{\boldsymbol{\tau}}\cdot(\hat{\mathbf{z}}\times\boldsymbol{g}_2)\mathbb{Z}]$. One can then show that $\overline{|\lambda, n, \alpha\rangle}$ forms a complete orthonormal basis of Hamiltonian (11) satisfying $\overline{\langle\lambda', n', \beta|\lambda, n, \alpha\rangle} = \delta_{\lambda\lambda'}\delta_{n'n}\delta_{\beta\alpha}$ (SM [18] Sec. S4A). Furthermore, $T_{\boldsymbol{D}_j+\boldsymbol{u}_\alpha-\boldsymbol{u}_\beta}$ is diagonal in λ and takes the λ independent form

$$T^{\lambda,\alpha\beta}_{\boldsymbol{D}_j+\boldsymbol{u}_\alpha-\boldsymbol{u}_\beta} = e^{-i(\hat{\boldsymbol{\kappa}}+\mathbf{k}_0)\cdot(\boldsymbol{D}_j+\boldsymbol{u}_\alpha-\boldsymbol{u}_\beta)} \tag{14}$$

in a fixed λ subspace between basis $\overline{|\lambda, n, \beta\rangle}$ and $\overline{|\lambda, n', \alpha\rangle}$, where $\hat{\boldsymbol{\kappa}} = \frac{1}{\sqrt{2}\ell}(a + a^\dagger, -ia + ia^\dagger)$, with $a\overline{|\lambda, n, \alpha\rangle} = \sqrt{n}\overline{|\lambda, n-1, \alpha\rangle}$ and $a^\dagger\overline{|\lambda, n, \alpha\rangle} = \sqrt{n+1}\overline{|\lambda, n+1, \alpha\rangle}$ (SM [18] Sec. S4A). Therefore, the nonzero-magnetic-field tight-binding Hamiltonian (11) in a fixed λ is given by the zero-field momentum space Hamiltonian (13) with substitution (5). For nonstandard Peierls substitutions along nonstraight $c_{\alpha\beta}$ paths, $e^{-i(\hat{\boldsymbol{\kappa}}+\mathbf{k}_0)\cdot(\boldsymbol{D}_j+\boldsymbol{u}_\alpha-\boldsymbol{u}_\beta)}$ in Eq. (14) becomes the path-ordered integral $\mathcal{P}e^{-i\int_{c_{\alpha\beta}}(\hat{\boldsymbol{\kappa}}+\mathbf{k}_0)\cdot d\mathbf{r}}$ (SM [18] Sec. S4B).

The Hofstadter butterfly can then be numerically calculated with a LL cutoff, namely, $n \leqslant N_L$. Figures 3(a) and 3(b) show the spectrum of the square lattice tight-binding model $H(\mathbf{k}) = -\cos k_x - \cos k_y$ [1] with cutoffs $N_L = 100$ and $N_L = 500$, respectively, where we set $\mathbf{k}_0 = \mathbf{0}$. The spectrum exhibits both the Hofstadter butterfly and the spectral flows, which can again be understood as momentum space edge states. Since tight-binding models have no cutoff in the reciprocal lattice, the momentum space boundary is always at radius $\kappa_b = \frac{\sqrt{2N_L}}{\ell}$ given by N_L, and the spectral flows always satisfy Eq. (9).

One can define a boundary projector $P_{\kappa_b,w}$ onto basis $\overline{|\lambda, n, \alpha\rangle}$ with $n > (\kappa_b - w)^2\ell^2/2$ for certain $w > 0$, and identify the eigenstates with $\langle P_{\kappa_b,w}\rangle > P_c$ for some $P_c \in [0, 1]$ as momentum space edge states. Figures 3(c) and 3(d) show the probability of a typical edge state and bulk state versus LL number n, respectively. By deleting the edge states, one can obtain a high-quality Hofstadter butterfly without spectral flows, as shown in Fig. 3(e) (where $w = 3.5\ell^{-1}\sqrt{\varphi + 0.5}$ and $P_c = 0.5$).

Quantized Lorentz susceptibility. The Chern number t_v is known to give a quantized Hall conductance via the Kubo formula $\sigma_{xy} = i\partial_\omega \int d\omega' \langle G_{\omega+\omega'}\hat{j}_x G_{\omega'}\hat{j}_y\rangle|_{\omega\to 0} = t_v\frac{e^2}{h}$ [10], where G_ω is the Green's function at energy ω, and $\hat{\boldsymbol{j}} = (\hat{j}_x, \hat{j}_y)$ is the uniform current operator. The duality between Eqs. (7) and (8) suggests that s_v behaves as a dual Chern number for the momentum space, thus s_v should also give a quantized response. Indeed, by noting that the natural momentum space dual of the current operator $\hat{\boldsymbol{j}}$ is the force operator $\hat{\boldsymbol{F}} = e\mathbf{B}\times\frac{d\mathbf{R}}{dt} = (\hat{F}_x, \hat{F}_y)$, we find s_v leads to a quantized *Lorentz susceptibility* (SM [18] Sec. S6)

$$\gamma_{xy} = -i\frac{\partial}{\partial\omega}\int d\omega' \langle G_{\omega+\omega'}\hat{F}_x G_{\omega'}\hat{F}_y\rangle\Big|_{\omega\to 0} = eBs_v. \tag{15}$$

It yields a Lorentz force per unit cell $F_x = \gamma_{xy}v_y$ on the system when the lattice is moving at velocity v_y. Furthermore, a formula similar to the Thouless–Kohmoto–Nightingale–den Nijs formula [10] at flux per unit cell $\varphi = 2\pi p/q$ can be derived for s_v (SM [18] Sec. S6B2),

$$s_v = -i\sum_{n\in\text{occ}}\int_{\boldsymbol{d}\in\Omega_M}\frac{d^2\boldsymbol{d}}{2\pi}\hat{\mathbf{z}}\cdot\langle\partial_{\boldsymbol{d}}w_{n,\boldsymbol{d}}|\times|\partial_{\boldsymbol{d}}w_{n,\boldsymbol{d}}\rangle, \tag{16}$$

where Ω_M is a torus with periods $\boldsymbol{d}_1$ and $\boldsymbol{d}_2/p$ serving as a "dual magnetic BZ," $|w_{n,\boldsymbol{d}}\rangle = e^{i\ell^{-2}(\hat{\mathbf{z}}\times\mathbf{R})\cdot\boldsymbol{d}}|\psi_{n,\ell^{-2}\hat{\mathbf{z}}\times\boldsymbol{d}}\rangle$ (see the explicit form in SM [18] Sec. S6C) is defined using the Bloch eigenstates $|\psi_{n,\mathbf{k}}\rangle$ of band n, and n runs over all occupied bands.

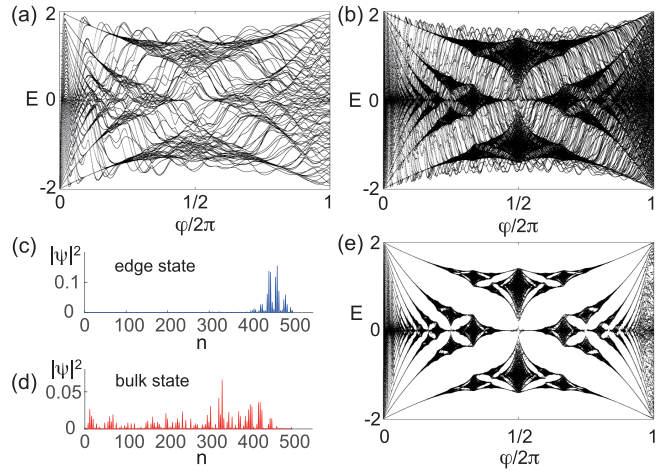

FIG. 3. The Hofstadter spectrum for tight-binding model $H(\mathbf{k}) = -\cos k_x - \cos k_y$ with $\mathbf{k}_0 = \mathbf{0}$ and LL cutoff (a) $N_L = 100$ and (b) $N_L = 500$. (c) Probability distribution of a typical momentum space edge state in (b) vs LL number n. (d) Probability distribution of a typical bulk state in (b). (e) The Hofstadter butterfly obtained by deleting the edge states in (b) (with $w = 3.5\ell^{-1}\sqrt{\varphi + 0.5}$, $P_c = 0.5$), which looks identical to that obtained by usual methods.

Discussion. It is worth noting that the cutoffs in our method affect the resolution but not the shape of the Hofstadter butterfly. Our method greatly simplifies the matrix element construction compared to usual methods [1,5], and require neither rational flux per unit cell nor large magnetic unit cells, making it easy to calculate the Hofstadter spectra of complicated models [12,24–26]. Moreover, it leads to a sparse Hamiltonian for continuum models. At small magnetic fields, our method reduces to the LL calculations of $\mathbf{k}\cdot\mathbf{p}$ Hamiltonians expanded at center momentum $\mathbf{k}_0$. The large magnetic field spectrum is insensitive to the choice of $\mathbf{k}_0$.

Acknowledgments. We thank Michael Zaletel, Hoi Chun Po, and Junyi Zhang for helpful discussions. B.L. acknowledge the support of Princeton Center for Theoretical Science at Princeton University at the early stage of this work. B.A.B was supported by the DOE Grant No. DE-SC0016239, the Schmidt Fund for Innovative Research, Simons Investigator Grant No. 404513, and the Packard Foundation. Further support was provided by the NSF-EAGER No. DMR 1643312, NSF-MRSEC No. DMR-1420541 and No. DMR-2011750, ONR No. N00014-20-1-2303, Gordon and Betty Moore Foundation through Grant No. GBMF8685 towards the Princeton theory program, BSF Israel U.S. foundation Grant No. 2018226, and the Princeton Global Network Funds.

[1] D. R. Hofstadter, Energy levels and wave functions of Bloch electrons in rational and irrational magnetic fields, Phys. Rev. B **14**, 2239 (1976).
[2] R. Bistritzer and A. H. MacDonald, Moiré bands in twisted double-layer graphene, Proc. Natl. Acad. Sci. USA **108**, 12233 (2011).
[3] J. M. B. Lopes dos Santos, N. M. R. Peres, and A. H. Castro Neto, Graphene Bilayer with a Twist: Electronic Structure, Phys. Rev. Lett. **99**, 256802 (2007).
[4] E. J. Mele, Commensuration and interlayer coherence in twisted bilayer graphene, Phys. Rev. B **81**, 161405(R) (2010).
[5] R. Bistritzer and A. H. MacDonald, Moiré butterflies in twisted bilayer graphene, Phys. Rev. B **84**, 035440 (2011).
[6] S. Janecek, M. Aichinger, and E. R. Hernández, Two-dimensional Bloch electrons in perpendicular magnetic fields: An exact calculation of the Hofstadter butterfly spectrum, Phys. Rev. B **87**, 235429 (2013).
[7] G. Gumbs, A. Iurov, D. Huang, and L. Zhemchuzhna, Revealing Hofstadter spectrum for graphene in a periodic potential, Phys. Rev. B **89**, 241407(R) (2014).
[8] K. Hejazi, C. Liu, and L. Balents, Landau levels in twisted bilayer graphene and semiclassical orbits, Phys. Rev. B **100**, 035115 (2019).
[9] Y.-H. Zhang, H. C. Po, and T. Senthil, Landau level degeneracy in twisted bilayer graphene: Role of symmetry breaking, Phys. Rev. B **100**, 125104 (2019).
[10] D. J. Thouless, M. Kohmoto, M. P. Nightingale, and M. den Nijs, Quantized Hall Conductance in a Two-Dimensional Periodic Potential, Phys. Rev. Lett. **49**, 405 (1982).
[11] R. Winkler, *Spin-Orbit Coupling Effects in Two-Dimensional Electron and Hole Systems*, Springer Tracts in Modern Physics (Springer, Berlin, 2003).
[12] B. Lian, F. Xie, and B. A. Bernevig, Landau level of fragile topology, Phys. Rev. B **102**, 041402(R) (2020).
[13] J. K. Asbóth and A. Alberti, Spectral Flow and Global Topology of the Hofstadter Butterfly, Phys. Rev. Lett. **118**, 216801 (2017).
[14] F. H. Claro and G. H. Wannier, Magnetic subband structure of electrons in hexagonal lattices, Phys. Rev. B **19**, 6068 (1979).
[15] I. Dana, Y. Avron, and J. Zak, Quantised Hall conductance in a perfect crystal, J. Phys. C **18**, L679 (1985).
[16] I. I. Satija, *Butterfly in the Quantum World* (Morgan & Claypool, San Rafael, CA, 2016).
[17] T. Kariyado and A. Vishwanath, Flat band in twisted bilayer Bravais lattices, Phys. Rev. Research **1**, 033076 (2019).
[18] See Supplemental Material at http://link.aps.org/supplemental/10.1103/PhysRevB.103.L161405 for details, which includes Refs. [27–31].
[19] G. H. Wannier, A result not dependent on rationality for Bloch electrons in a magnetic field, Phys. Status Solidi B **88**, 757 (1978).
[20] P. Streda, Theory of quantised Hall conductivity in two dimensions, J. Phys. C **15**, L717 (1982).
[21] J. M. Luttinger, The effect of a magnetic field on electrons in a periodic potential, Phys. Rev. **84**, 814 (1951).
[22] T. Kita and M. Arai, Theory of interacting Bloch electrons in a magnetic field, J. Phys. Soc. Jpn. **74**, 2813 (2005).
[23] A. Alexandradinata and L. Glazman, Semiclassical theory of Landau levels and magnetic breakdown in topological metals, Phys. Rev. B **97**, 144422 (2018).
[24] J. Herzog-Arbeitman, Z.-D. Song, N. Regnault, and B. A. Bernevig, Hofstadter Topology: Noncrystalline Topological Materials at High Flux, Phys. Rev. Lett. **125**, 236804 (2020).
[25] X. Lu, B. Lian, G. Chaudhary, B. A. Piot, G. Romagnoli, K. Watanabe, T. Taniguchi, M. Poggio, A. H. MacDonald, B. A. Bernevig, and D. K. Efetov, Multiple flat bands and topological Hofstadter butterfly in twisted bilayer graphene close to the second magic angle, arXiv:2006.13963.
[26] G. W. Burg, B. Lian, T. Taniguchi, K. Watanabe, B. A. Bernevig, and E. Tutuc, Evidence of emergent symmetry and valley Chern number in twisted double-bilayer graphene, arXiv:2006.14000.
[27] A. L. Sharpe, E. J. Fox, A. W. Barnard, J. Finney, K. Watanabe, T. Taniguchi, M. A. Kastner, and D. Goldhaber-Gordon, Emergent ferromagnetism near three-quarters filling in twisted bilayer graphene, Science **365**, 605 (2019).
[28] M. Serlin, C. L. Tschirhart, H. Polshyn, Y. Zhang, J. Zhu, K. Watanabe, T. Taniguchi, L. Balents, and A. F. Young, Intrinsic quantized anomalous Hall effect in a moiré heterostructure, Science **367**, 900 (2020).
[29] Z. Song, Z. Wang, W. Shi, G. Li, C. Fang, and B. A. Bernevig, All Magic Angles in Twisted Bilayer Graphene are Topological, Phys. Rev. Lett. **123**, 036401 (2019).
[30] B. A. Bernevig and T. L. Hughes, *Topological Insulators and Topological Superconductors* (Princeton University Press, Princeton, NJ, 2013).
[31] R. Karplus and J. M. Luttinger, Hall effect in ferromagnetics, Phys. Rev. **95**, 1154 (1954).